Soft Matter

COMMUNICATION

View Article Online
View Journal | View Issue

Cite this: *Soft Matter*, 2014, **10**, 5243

Self-assembly in an evaporating nanofluid droplet: rapid transformation of nanorods into 3D fibre network structures†

Received 23rd April 2014
Accepted 2nd June 2014

DOI: 10.1039/c4sm00887a

www.rsc.org/softmatter

H. Wu,[a] L. X. Chen,[a] X. Q. Zeng,[b] T. H. Ren*[a] and Wuge H. Briscoe*[c]

Upon evaporation, ZnO nanorods in a nanofluid droplet undergo rapid and spontaneous chemical and morphological transformation into centimetre-long $Zn(OH)_2$ fibres, *via* a mechanism very different from that for *coffee rings*. We show that the detailed nanostructure and micromorphology in the residual thin film depend intricately on the ambient moisture, nanofluid solvent composition and substrate surface chemistry. Upon thermal annealing, these $Zn(OH)_2$ fibres readily undergo further chemical and morphological transformation, forming nanoporous fibres with the pore size tuneable by temperature. Our results point to a simple route for generating a self-assembled 3D structure with ultralong and nanoporous ZnO/$Zn(OH)_2$ fibres/belts, and may also be of interest to the fields of evaporation controlled dynamic self-assembly, non-equilibrium crystallisation, and flow and fingering instabilities in nanofluids.

The residual surface pattern from the evaporative drying process of a particle-laden droplet is a manifestation of the delicate, temporally and spatially fluctuating balance between capillary and Marangoni flows in the droplet,[1–8] and this balance may be tuned by manipulating parameters such as droplet surface tension,[9] particle concentration,[10] size and shape,[11] inter-particle forces[12] and physical confinement.[13] Whilst a commonly observed pattern is that of the *coffee ring*, a peripheral ring deposit formed at the pinned droplet wetting line, various other 2D and 3D structures have been produced, including multiple rings,[14] regular stripes,[13,15–17] multilayer deposits,[18] and uniform deposits.[11,19] Understanding the physical mechanisms that underpin the formation of these surface structures is crucial to controlling and optimizing their morphologies for applications ranging from biomedical assays, to electronic circuit printing and to templated fabrication of higher-order nanostructures.[12,17,18,20]

Here we demonstrate that uniform thin films with self-assembled 3D network structures consisting of ultra-long fibres can rapidly form on a surface from evaporative drying of a droplet of ZnO nanorod dispersion. We elucidate that the mechanism for this process is very different from that previously established for the coffee ring effect: it involves initial moisture-assisted rapid dissolution of ZnO nanorods and subsequent formation of long $Zn(OH)_2$ fibres *via* a nonequilibrium crystallization process, which induces fingering instabilities at dewetting front of the drying droplet and, in turn, guides and promotes self-assembly of the $Zn(OH)_2$ fibres. We show that, upon subsequent heat treatment, the 3D $Zn(OH)_2$ fibre networks readily undergo structural and chemical transformation to porous fibres comprising ZnO nanoparticles of size 4–7 nm, and we further show that the structural details of such 3D $Zn(OH)_2$ fibre networks depend intricately on the wettability of the substrate. Our finding provides a facile route for producing fibre networks and porous fibre/belt coatings.

To prepare ZnO nanorods, 0.015 mol zinc acetate and 3 mL octylamine were added to 150 mL triethylene glycol. This reaction mixture was transferred to a Teflon-lined stainless steel autoclave and heated at 190 °C for 8 h. The precipitated ZnO nanorods were then washed twice using methanol and recovered by freeze-drying. The diameter and length of ZnO nanorod was 25–50 nm and 50–200 nm, respectively (Fig. 1a). Nanorods were then dispersed in desired solvent mixtures by sonication to give final centration in the range 1–100 mg mL^{-1}. For evaporation experiments, a nanorod-containing droplet of certain volume and solvent composition was drop-cast on a glass coverslip surface by a micro-syringe, then evaporation occurred naturally under 25 °C and controlled relative humidity (RH). Typically this evaporative drying process completes in ~3 min.

Fig. 1b shows an example image of a circular shaped deposit pattern of diameter ~1.5 cm after drying of a 50 μL droplet with 1 mg mL^{-1} ZnO nanorod (25–50 nm in diameter × 50–200 nm

[a]*School of Chemistry and Chemical Engineering, Shanghai Jiao Tong University, Shanghai 200240, PR China. E-mail: thren@sjtu.edu.cn*

[b]*Laboratory for Surface Technology and Tribology, Faculty of Engineering Technology, University of Twente, Enschede, The Netherlands*

[c]*School of Chemistry, University of Bristol, Cantock's Close, Bristol BS8 1TS, UK. E-mail: wuge.briscoe@bristol.ac.uk*

† Electronic supplementary information (ESI) available. See DOI: 10.1039/c4sm00887a

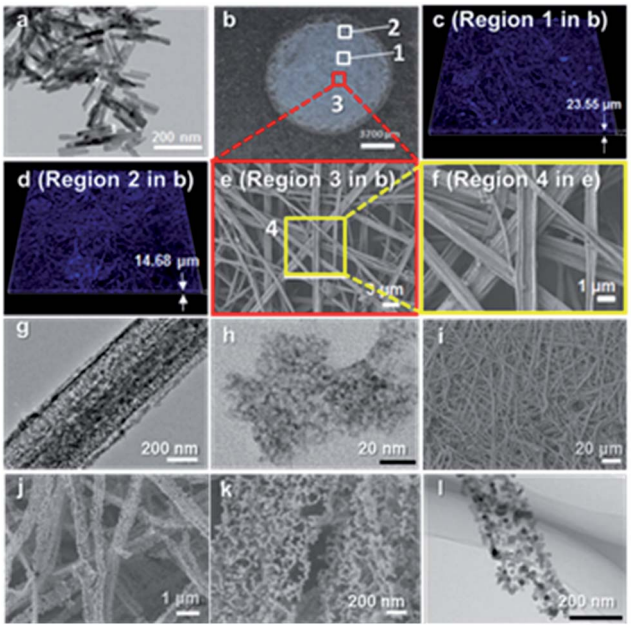

Fig. 1 (a) TEM image of ZnO nanorods; (b) photograph of a circular shaped thin film deposit after drying of a 50 μL droplet with 1 mg mL^{-1} ZnO suspension in a mixture of cyclohexane and isobutylamine in a ratio 5 : 1 on a glass coverslip surface; (c and d) confocal microscope images of Regions 1 and 2 in (b); (e) enlarged view of region 3 in (b); (f) enlarged view of region 4 in (e); (g and h) TEM images of an individual fibre and its constituent nanocrystals; (i–k) SEM images of the 3D fibre networks calcined at 550 °C at different magnifications; (l) TEM image of an individual fibre calcined at 550 °C. To obtain the TEM images in (g and l) the carbon-coated TEM grid was directly adhered to 3D fibres network on the glass coverslip surface. For (h) the fibres were dispersed in ethanol by sonication and then drop-casted on the carbon-coated TEM grid surface.

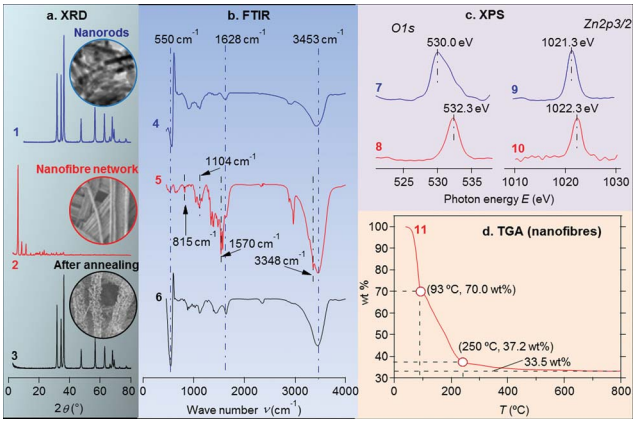

Fig. 2 Powder X-ray diffraction (XRD) patterns (a), Fourier transform infrared (FTIR) spectra (b) and X-ray photoelectron spectra (XPS) (c) for ZnO nanorods (blue curves) and $Zn(OH)_2$ fibres (red curves). XRD and FTIR data are also shown for the fibres annealed at 550 °C (black curves). (d) Thermogravimetry analysis (TGA) curve for the fibres.

in length; Fig. 1a) dispersion in a mixture of cyclohexane and isobutylamine with a volume ratio $V_c : V_i = 5 : 1$ on a glass coverslip (24 mm × 24 mm) at ambient relative humidity (RH) ~65%. The deposit appears as a uniform coating of thickness 14–25 μm (Fig. 1c and d) clearly different from the commonly observed coffee ring pattern from a drying droplet.[1–4] Fig. 1e reveals a 3D crisscrossed network structure in the film, consisting of fibres (or ultralong belts) of width 0.5–2 μm (Fig. 1f) with a tube-groove morphology, *i.e.* the long edges of the fibre are curved upwards resembling bamboo stems truncated along the length. SEM scanning reveals that some fibres stretch continuously across the full width of the circular deposit, thus with fibre lengths up to ~1.5 cm. Increasing the ZnO nanorod concentration in the droplet leads to thinner fibres but a denser network (Fig. S1†). In particular, the deposit pattern after drying a 400 μL droplet of 100 mg mL^{-1} ZnO nanorod suspension appears a uniform thick film (Fig. S1g†). Surprisingly, TEM images (Fig. 1g and h) reveal that the self-assembled fibres have a uniform, dense distribution of 3–5 nm *nanocrystals*, whose lattice fringes are observable in the HRTEM image in Fig. S2,† instead of the ZnO *nanorods* in the original droplet (Fig. 1a).

The powder X-ray diffraction (XRD) pattern of the self-assembled fibres (red curve 2 in Fig. 2a) is very different from that of ZnO nanorods (blue curve 1 in Fig. 2a); instead, it is reminiscent of layered basic zinc salt (LBZS), such as $Zn(OH)_{1.6}(CH_3COO)_{0.4}\cdot 0.6H_2O$ [21] and $Zn(OH)_{1.75}(CH_3COO)_{0.26}\cdot 0.57H_2O$.[22] The Fourier transform infrared (FTIR) spectrum for the fibres (red curve 5 in Fig. 2b) shows unequivocally the presence of isobutylamine and hydroxyl groups, but the peak at about 557 cm^{-1}, characteristic of ZnO (the black curve in Fig. S3b†), is absent from the spectrum. This concurs with the XRD results above that the constituent nanocrystals for the fibres are not ZnO. The X-ray photoelectron spectroscopy (XPS) analysis reveals the chemical structure of the self-assembled fibres (red curves 8 and 10 in Fig. 2c), with peaks centered around 532.3 and 1022.3 eV attributed to O1s and $Zn2p_{3/2}$ of $Zn(OH)_2$,[23] respectively; whereas the corresponding peaks for the ZnO nanorods are observed at 530.0 and 1021.3 eV, respectively (blue curves 7 and 9 in Fig. 2c). This result further confirms that the nanocrystals in the fibres are not ZnO nanorods; rather, they are $Zn(OH)_2$ nanocrystals – formed, we suggest, as a result of the rapid dissolution of ZnO nanorods and subsequent re-crystallisation during droplet drying. Thermogravimetry analysis (TGA) of the self-assembled fibres conducted in a flowing air atmosphere shows a first weight loss of ~30% due to evaporation of isobutylamine in the temperature range 25–93 °C (red curve 11 in Fig. 2d). A second weight loss of 33% in the range 93–250 °C corresponds to the removal of water, physisorbed and intercalated into $Zn(OH)_2$ nanocrystal layers, and a further weight loss of 3.7% in the range 250–800 °C is attributed to loss of chemically bound water.

The $Zn(OH)_2$ fibres can undergo structural and chemical transformation under simple thermal treatment, giving rise to a 3D network structure comprising nanoporous fibres constituting a pure hexagonal ZnO phase with a wurtzite structure (Fig. S3†). The XRD pattern (black curve 3 in Fig. 2a) and FTIR spectrum (black curve 6 in Fig. 2b) of the $Zn(OH)_2$ fibres annealed at 550 °C are characteristic of ZnO. TEM images show that, for the samples annealed at 100 and 250 °C (Fig. S4a

and c†), the fibres are composed of ZnO nanocrystals of size 4–7 nm (Fig. S4b and d†); whereas for the 550 °C sample (Fig. 1i–k), discrete ZnO nanoparticles of size 20–70 nm are clearly visible in the fibre (Fig. 1l), with gaps/pores between the nanocrystals vacated by the evaporation of isobutylamine and water molecules. Elevated annealing temperature may have promoted rearrangement and realignment of the nanocrystals, with smaller ZnO nanocrystals also sintered into larger ones. Thus, the structure of the fibre becomes increasingly porous as the pore size increases with the annealing temperature. Although some fibre breakage is observed due to thermal stress, the 3D fibre network is retained without collapsing after calcination. Such structural integrity may be attributed to multiple contacts between nanoparticles in the network that would stabilise the structure.

A key step in the rapid formation of the 3D fibre network structure is the dissolution of isobutylamine-coated nanorods that later form layered $Zn(OH)_2$ nanocrystals, and it is thus crucial to establish the timing of the dissolution process. Firstly, we note that no $Zn(OH)_2$ aggregates can be observed by TEM from ZnO isobutylamine-coated nanorod samples after storage in sealed glass vials at room temperature for 21 days (Fig. S5†). By contrast, as shown in the TEM images (Fig. 3a–c) of the constituent nanostructures of the droplets harvested at different time intervals (60, 385 and 900 s) of the drying process of a droplet of ZnO nanorod dispersion in the cyclohexane–isobutylamine (5 : 1) mixture, the dissolution of ZnO nanorods occurs rapidly during the process, with nanocrystals appearing on the carbon-coated TEM grid surface for the evaporation time as short as 1 min (Fig. 3a) and their dissolution almost completed after 900 s (Fig. 3c).

To assess the role of moisture in the formation of fibre networks, the above evaporation process of the droplet is repeated in a sealed glove box of volume 280 L with a controlled relative humidity (RH). At RH below 10%, a uniform layer of film, consisting of ZnO nanorods coated by $Zn(OH)_2$ nanocrystals, is observed on the glass coverslip at the end of evaporation (Fig. 3d; see also Fig. S6†). At RH ~30%, there is a coexistence of short fibres, ZnO nanorods and large aggregates of ZnO nanorods (Fig. 3e). With the RH increased to 60% and above, 3D ultralong fibre networks are observed without any undissolved ZnO nanorods (Fig. 3f). The results indicate that ambient water molecules play a crucial role in the dissolution of ZnO nanorods, and fibres would form only at RH > ~60%.

Equally important to the fibre formation is the solvent composition (*i.e.* the volume ratio $V_c : V_i$ between cyclohexane and isobutylamine). When the evaporation process is performed at the volume ratio $V_c : V_i = 50 : 1$ and 1 : 10 (instead of 5 : 1) and also from a droplet with pure isobutylamine as the solvent, no ultra-long fibres are formed; instead, a range of micro-morphologies are observed (Fig. 3g–i; see also Fig. S7†) including fibre-rod mixtures and densely packed or isolated dendritic patterns.

Based on the timing of the dissolution process (Fig. 3a–c), the micro-morphologies of residual patterns obtained at different RHs (Fig. 3d–f) and different solvent compositions (Fig. 3g–i), and the corroborating evidence from our structural analyses (Fig. 1, 2 and S3†), we propose the following mechanism for ZnO nanorod dissolution and $Zn(OH)_2$ fibre network formation from evaporative drying of a ZnO nanorod-containing droplet. Once the droplet is cast on the substrate surface, water molecules from air are promptly taken up due to the miscibility of isobutylamine with water, and also become entrained to the surface of isobutylamine-coated ZnO nanorods where reaction (1) may be initiated,

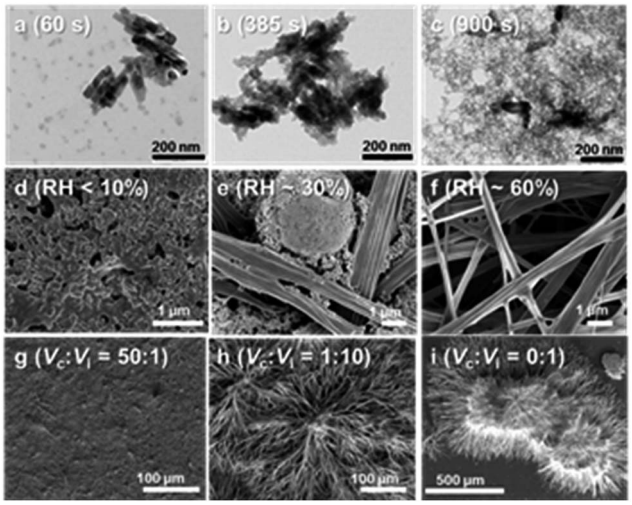

Fig. 3 TEM images (a–c) of the constituent nanostructures of evaporating droplets at different time intervals during the drying process (60, 385 and 900 s after initial drop-casting respectively). (d–l) SEM images of the deposit micro-morphologies from a 400 μL ZnO (1 mg mL^{-1}) nanofluid droplet evaporated under different conditions: different RHs (<10% (d), 35% (e), 60% (f), with a drying time of ~12, 15 and 20 min respectively); with different cyclohexane/isobutylamine volume ratios ($V_c : V_i$) of 50 : 1 (g), 1 : 10 (h) and 0 : 1 (pure isobutylamine) (i) – all on glass coverslip and at ambient RH ~65%. The sample preparation procedure for results shown in Fig. 3a–c is as follows. A 200 μL droplet with 1 mg mL^{-1} ZnO dispersion is drop-casted on the glass coverslip surface by a micro-syringe. The solvent is a mixture of cyclohexane and isobutylamine in a 5 : 1 ratio. For the sample in Fig. 3a, the evaporation time of the ZnO nanorod suspension on the glass coverslip is 1 min, where evaporation is incomplete and the droplet remains a fluid drop. The glass coverslip with the wet droplet is then immediately submerged into a bottle containing 40 mL ethanol, enclosed with a lid, and then sonicated for 30 min. Ten droplets, each of 2 μL in volume are cast on the carbon-coated TEM grid, and an example of the obtained TEM images is shown in (a). The TEM samples for (b) is prepared, when the evaporation time for the sample in Fig. 3b is about 385 s, at which the evaporative dewetting front recedes to the centre of the droplet, leaving behind a thick layer of viscous sol (or gel). The sample for Fig. 3c is obtained by the similar procedure after the solvent has completely evaporated.

$$\text{i-}C_4H_{11}N + H_2O \leftrightarrow \text{i-}C_4H_{12}N^+ + OH^- \quad (1)$$

Subsequently, the (0001) plane of ZnO at the tip of the nanorods is likely to be dissolved first, due to its weak alkalinity,[24,25]

$$ZnO_{(s)} + \text{i-}C_4H_{12}N^+ + OH^- + H_2O \leftrightarrow Zn(OH)_3^- \cdot {}^+\text{Ni-}C_4H_{12(aq)} \quad (2)$$

and evidence for such partially dissolved ZnO rods is shown in Fig. S8.† Liquid $Zn(OH)_3^- \cdot {}^+Ni\text{-}C_4H_{12}$ is transported away from the rods by convective flow, allowing further dissolution of ZnO rods, a process sustained by water present. As the evaporation proceeds, crystallization into $Zn(OH)_2$ crystals *via* reaction (3) is initiated at the liquid–air interface towards the edge of the droplet, where the solution reaches its saturation point first,

$$Zn(OH)_3^- \cdot {}^+Ni\text{-}C_4H_{12(aq)} \leftrightarrow Zn(OH)_{2(s)} + i\text{-}C_4H_{11}N + H_2O \quad (3)$$

A key question remains: what are the driving forces for $Zn(OH)_2$ nanocrystals to assemble into long fibres? We suggest that, the solvent evaporation of isobutylamine–cyclohexane mixture, crystallization-mediated fingering instabilities at dewetting front of the evaporating droplet and inter-nanocrystal H-bonding, corroborate to lead to the ultimate fibril morphology. Due to its surface activity and rapid evaporation of isobutylamine, the solutes, including liquid $Zn(OH)_3^- \cdot {}^+Ni\text{-}C_4H_{12}$ and undissolved ZnO nanorods, tends to localize and concentrate near the liquid–air interface, where $Zn(OH)_2$ crystallization is always initiated and three-phase (solution/wet $Zn(OH)_2$ nanocrystals/air) contact lines consequently form and recede in the fibre growth direction as evaporation dewetting proceeds. Due to the surface tension gradient caused by rapid solvent evaporation and concentration gradient in the vicinity of nonequilibrium crystallization growth, *fingering instabilities* are triggered at receding evaporative dewetting front,[26–29] with 3D fingers originating from multiple crystallization sites at the droplet surface and its circumference on the substrate and propagating inwards. The newly formed $Zn(OH)_2$ platelets coated with isobutylamine and water interact and bind with each other *via* H-bonding; whilst $Zn(OH)_3^- \cdot {}^+Ni\text{-}C_4H_{12}$ in its supersaturated isobutylamine solution is driven towards and into the growth front of the fingers, effectively localizing (or jamming) $Zn(OH)_2$ platelets at the finger front through continued crystallization and facilitating the growth of fingers into quasi-fibre networks (Fig. S9c and d†). This process would propagate from the edge to the centre of the droplet and from the liquid–air interface towards the substrate surface as evaporation proceeds to completion, leading to the transition of quasi-fibre network structure into the ultimate 3D centimeter-long fibre network structure. The role of the solvent composition in this mechanism is pivotal: it governs the crystallization dynamics and the fingering instabilities of evaporative dewetting front, leading to various morphologies and structures of the deposit patterns. Here we have used ZnO nanorods, whose crystal structure plays a role in the initial dissolution process, and the size and geometry of the nanostructures would also contribute to the subsequent flow dynamics through their interplay with the solvent. Our initial results using ZnO nanoparticles indeed show different residual patterns and micromorphologies (H. Wu *et al. in preparation*), pointing to further versatility of this simple route in obtaining hierarchical surface patterns.

The afore-proposed mechanism for the 3D fibre network formation suggests that nonequilibrium factors, such as evaporation flux, nonequilibrium crystallisation and convection, play an important role in guiding the fibre self-assembly process. During the evaporation of a droplet of radius R, the evaporating flux $J(r)$ at a distance r from droplet centre scales as $J(r) \propto (R - r)^{\lambda}$, where $\lambda = (\pi - 2\theta)/(2\pi - 2\theta)$ with θ the contact angle that the droplet makes with the substrate at the three-phase contact line.[30] This indicates that the solvent evaporation dynamics close to the surface, particularly at the dewetting front, during evaporation is influenced by the surface wettability by the dispersion, and thus the surface chemistry of the substrate. Fig. 4 shows SEM images of 3D fibre network formed under the same conditions on various substrates. Indeed, the microscopic and nanoscopic morphologies of the fibres of the network depend sensitively on the nature of the substrate used. SEM images at lower magnification (Fig. 4, left hand side column) show that all the deposit patterns on the various substrates present a 3D network structure comprising self-assembled by fibres, clearly different from previously reported structures of the coffee ring, central dump or hexagonal arrays for drying droplets.[1–4,31] At

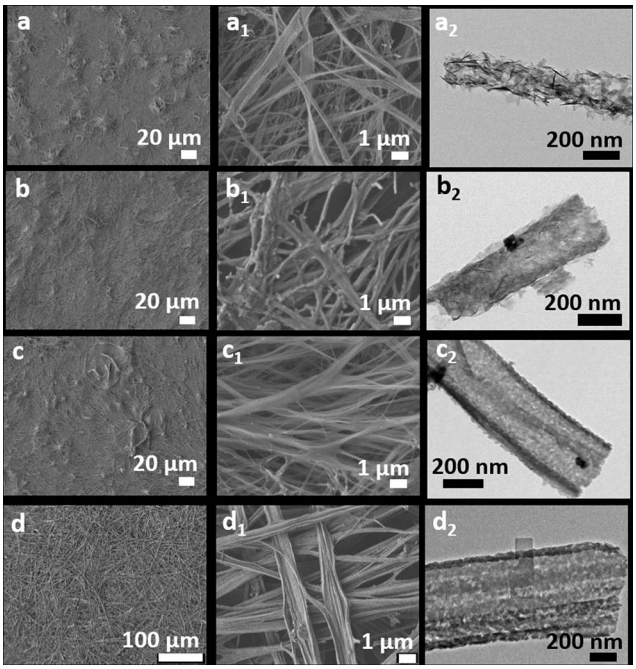

Fig. 4 SEM images of 3D fibre network structure and TEM images of individual fibres on various solid substrates: (a, a_1, and a_2) a mica sheet; (b, b_1, and b_2) a polytetrafluoroethylene (PTFE) sheet; (c, c_1, and c_2) a silicon wafer; and (d, d_1, and d_2) a glass coverslip. The sample preparation procedures for these samples are identical: a droplet of 400 μL ZnO nanorod suspensions is drop casted on the substrate surface (24 mm × 24 mm), with other experimental conditions the same as those of the samples in Fig. 1. After the completion of solvent evaporation, TEM images are obtained by directly adhering carbon-coated TEM grid on the surface of the final 3D network films. The silicon wafer and the PTFE sheet are first cleaned by piranha (30% H_2O_2 + 70% H_2SO_4 by volume), rinsed with water, followed by methanol by sonication. The mica sheet and glass coverslip are untreated. The contact angles(θ) on these four substrates are 13.5° (silicon wafer), 20.3° (PTFE), 10.2° (mica) and 12.2° (glass coverslip), measured by placing a 2 μL droplet with 1 mg mL^{-1} ZnO suspension in a mixture of cyclohexane and isobutylamine in a ratio 5 : 1 on these substrates.

the high SEM magnification (Fig. 4, middle column), 3D crisscrossed networks on the glass coverslip surface appear denser than those on the other three substrates. TEM images of the nanoscopic structure of an individual fibre from the 3D network on these four different substrates are presented in right hand column in Fig. 4. Interestingly, for mica and the polytetrafluoroethylene substrate, ultrathin $Zn(OH)_2$ nanocrystal sheets are clearly visible in the fibre (Fig. $4a_2$ and b_2). $Zn(OH)_2$ nanocrystals in the fibres on mica (Fig. $4a_2$) are randomly packed and loosely stacked in a face-to-edge configuration; whereas they are more densely packed on other three substrates (Fig. $4b_2$, c_2 and d_2). Thus, varying surface chemistry of the substrate provides a simple route for tuning the structure and morphology of the self-assembled 3D fibre networks. In addition to the local flux which controls the dynamics of the dewetting front and the resulted fingering instability, the ultimate micromorphologies in the residual surface deposit also depend sensitively on the global flux, controlled by evaporation time (or rate). For instance, the interpretation of the effect of RH is convoluted with that of the evaporation rate, as discussed in a forthcoming ms.

In summary, we show that the residual surface pattern from a drying ZnO-nanofluid droplet consists of a uniform film with the structure of 3D fibre networks, which is very different from the commonly observed coffee rings. We propose a mechanism for the rapid and spontaneous formation of the fibre networks, in which evaporation induced dissolution of ZnO nanorods and re-crystallisation of $Zn(OH)_2$ at the evaporating dewetting front are dominant factors governing the formation of ultra-long fibre networks. Our results point to a simple route for generating self-assembled 3D structure with ultralong fibres/belts, important to a range of modern technologies, such as piezoelectric transducers and actuators, solar cells, acoustic-optical devices, and biomedical sensors in which ZnO and related materials are employed.[32–34] Our results may also be of general interest to the fields of evaporation controlled dynamic self-assembly, fibre formation, non-equilibrium crystallisation, and flow and fingering instabilities in nanofluids.

Acknowledgements

We would like to M. N. R. Ashfold (Bristol Chemistry) for suggesting the experiments on varying relative humidities. HW would like to acknowledge funding from CSC (China) and Natural Science Foundation of Shanghai City (12ZR1413400). WHB would like to acknowledge funding from the EPSRC (EP/H034862/1 and Building Global Engagement in Research (BGER)), the Royal Society (UK), the Taiho Kogyo Tribology Research Foundation (TTRF), the European Research Council (ERC), European Cooperation in Science and Technology (CMST COST) Action CM1101 "Colloidal Aspects of Nanoscience for Innovative Processes and Materials", and Marie Curie Initial Training Network (MCITN) on "Soft, Small, and Smart: Design, Assembly, and Dynamics of Novel Nanoparticles for Novel Industrial Applications" (*NanoS3*).

Notes and references

1 R. D. Deegan, O. Bakajin, F. T. Dupont, G. Huber, S. R. Nagel and T. A. Witten, *Nature*, 1997, **389**, 827–829.
2 R. D. Deegan, O. Bakajin, F. T. Dupont, G. Huber, S. R. Nagel and T. A. Witten, *Phys. Rev. E: Stat. Phys., Plasmas, Fluids, Relat. Interdiscip. Top.*, 2000, **62**, 756–765.
3 E. Rabani, D. R. Reichman, P. L. Geissler and L. E. Brus, *Nature*, 2003, **426**, 271–274.
4 D. Kuncicky and O. Velev, *Langmuir*, 2008, **24**, 1371–1380.
5 B. Philip, in *The Self-Made Tapestry: Pattern Formation in Nature*, Oxford University Press, Oxford, 1999.
6 A. F. Routh, *Rep. Prog. Phys.*, 2013, **76**, 046603.
7 W. Han and Z. Lin, *Angew. Chem., Int. Ed.*, 2012, **51**, 1534–1546.
8 R. G. Larson, *Angew. Chem., Int. Ed.*, 2012, **51**, 2546–2548.
9 T. P. Bigioni, X. M. Lin, T. T. Nguyen, E. I. Corwin, T. A. Witten and H. M. Jaeger, *Nat. Mater.*, 2006, **5**, 265–270.
10 H. M. Ma and J. C. Hao, *Chem.–Eur. J.*, 2010, **16**, 655–660.
11 P. Yunker, T. Still, M. Lohr and A. Yodh, *Nature*, 2011, **476**, 308–311.
12 B. Rajneesh, X. H. Fang, S. Ponisseril and A. Daniel, *Langmuir*, 2010, **26**, 7833–7842.
13 J. Xu, J. F. Xia and Z. Q. Lin, *Angew. Chem., Int. Ed.*, 2007, **46**, 1860–1863; *Angew. Chem.*, 2007, **119**, 1892–1895.
14 L. Shmuylovich, A. Shen and H. Stone, *Langmuir*, 2002, **18**, 3441–3445.
15 H. Bodiguel, F. Doumenc and B. Guerrier, *Langmuir*, 2010, **26**, 10758–10763.
16 Y. J. Cai and B. M. Newby Zhang, *J. Am. Chem. Soc.*, 2008, **130**, 6076–6077.
17 J. X. Huang, F. Kim, A. R. Tao, S. Connor and P. Yang, *Nat. Mater.*, 2005, **4**, 896–900.
18 H. Hu and R. Larson, *J. Phys. Chem. B*, 2006, **110**, 7090–7094.
19 E. Ng, K. Chin and C. Wong, *Langmuir*, 2011, **27**, 2244–2249.
20 H. B. Eral, D. M. Augustine, M. H. G. Duits and F. Mugele, *Soft Mater.*, 2011, **7**, 4954–4958.
21 L. Poul, N. Jouini and F. Fiévet, *Chem. Mater.*, 2000, **12**, 3123–3132.
22 R. Q. Song, A. W. Xu, B. Deng, Q. Li and G. Y. Chen, *Adv. Funct. Mater.*, 2007, **17**, 296–306.
23 G. Deroubais and P. Marcus, *Surf. Interface Anal.*, 1992, **18**, 39–46.
24 B. P. Renee, L. F. Clark and A. G. Brian, *Langmuir*, 2004, **20**, 5114–5118.
25 R. A. Laudise and A. A. Ballman, *J. Phys. Chem. B*, 1960, **64**, 688–691.
26 I. Vancea and U. Thiele, *Phys. Rev. E: Stat., Nonlinear, Soft Matter Phys.*, 2008, **78**, 041601.
27 E. Pauliac-Vaujour, A. Stannard, C. P. Martin, M. O. Blunt, I. Notingher, P. J. Moriarty, I. Vancea and U. Thiele, *Phys. Rev. Lett.*, 2008, **100**, 176102.
28 U. Thiele, I. Vancea, A. J. Archer, M. J. Robbins, L. Frastia, A. Stannard, E. P. Vaujour, C. P. Martin, M. O. Blunt and P. J. Moriarty, *J. Phys.: Condens. Matter*, 2009, **21**, 264016.
29 M. Maillard, L. Motte and M. P. Pileni, *Adv. Mater.*, 2001, **13**, 200–204.

30 N. N. Jason, R. G. Chaudhuri and S. Paria, *Soft Matter*, 2012, **8**, 3771–3780.
31 R. Bhardwaj, X. Fang and D. Attinger, *New J. Phys.*, 2009, **11**, 075020.
32 Q. F. Zhang, C. S. Dandeneau, X. Y. Zhou and G. Z. Cao, *Adv. Mater.*, 2009, **21**, 4087–4108.
33 W. Z. Wang, B. Q. Zeng, J. Yang, B. Poudel, J. Y. Huang, M. J. Naughton and Z. F. Ren, *Adv. Mater.*, 2006, **18**, 3275–3278.
34 R. S. Devan, R. A. Patil, J. H. Lin and Y. R. Ma, *Adv. Funct. Mater.*, 2012, **22**, 3326–3370.